

# Observational inferences of lateral eddy diffusivity in the halocline of the Beaufort Gyre

Gianluca Meneghello<sup>1</sup>, John Marshall<sup>1</sup>, Sylvia T. Cole<sup>2</sup>, and Mary-Louise Timmermans<sup>3</sup>

<sup>1</sup>Department of Earth, Atmospheric and Planetary Sciences, Massachusetts Institute of Technology, Cambridge, Massachusetts, USA

<sup>2</sup>Woods Hole Oceanographic Institution, Woods Hole, Massachusetts, USA

<sup>3</sup>Department of Geology and Geophysics, Yale University, New Haven, Connecticut, USA,

## Key Points:

- Eddy diffusivity in the Beaufort Gyre (BG) ranges from 100-500 m<sup>2</sup> s<sup>-1</sup> near the surface, decaying rapidly with depth across the halocline
- Eddy-induced upwelling largely compensates downward Ekman pumping in the BG
- Lateral eddy diffusivity plays a zero-order role in the freshwater budget of the BG

---

Corresponding author: Gianluca Meneghello, gianluca.meneghello@gmail.com

**Abstract**

Using Ekman pumping rates mediated by sea-ice in the Arctic Ocean’s Beaufort Gyre (BG), the magnitude of lateral eddy diffusivities required to balance downward pumping is inferred. In this limit — that of vanishing residual-mean circulation — eddy-induced upwelling exactly balances downward pumping. The implied eddy diffusivity varies spatially with values of 50-400  $\text{m}^2 \text{s}^{-1}$ , and decays with depth. Eddy diffusivity estimated using mixing length theory applied to BG mooring data exhibits a similar range of values from 100  $\text{m}^2 \text{s}^{-1}$  to more than 600  $\text{m}^2 \text{s}^{-1}$ , and also decays with depth. We conclude that eddy diffusivities in the BG are likely large enough to balance downward Ekman pumping, arresting the deepening of the gyre and suggesting that eddies play a zero-order role in buoyancy and freshwater budgets of the BG.

**1 Introduction**

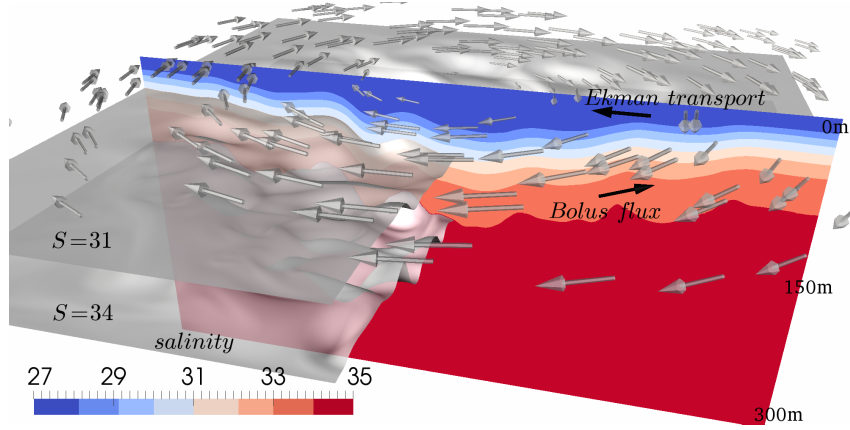
The Arctic Ocean’s Beaufort Gyre, centered in the Canada Basin, is characterized by a strong halocline stratification with relatively fresh surface waters overlying saltier (and warmer) waters of Atlantic Ocean origin. The halocline stratification inhibits the vertical flux of ocean heat to the overlying sea-ice cover. The halocline is deepened by Ekman pumping associated with a persistent but highly variable Arctic high pressure system [Proshutinsky and Johnson, 1997; Proshutinsky *et al.*, 2009, 2015]. This creates the anticyclonic Beaufort Gyre (BG) in which salinity surfaces bow downwards creating a bowl of freshwater, the main reservoir of freshwater in the Arctic.

Due to the store of available potential energy associated with its tilted isopycnal surfaces, the BG is highly susceptible to baroclinic instability and indeed a ubiquitous mesoscale eddy field is a notable feature of observations [Manley and Hunkins, 1985; Timmermans *et al.*, 2008; Zhao *et al.*, 2014, 2016].

Through idealized modeling studies, the mesoscale eddy field, which includes coherent eddies (of order 10 km in diameter) as well as fluctuations on order 100 km scales, has been implicated in playing a key role in equilibrating the freshwater budget of the BG [Manucharyan *et al.*, 2016; Manucharyan and Spall, 2016]. However it is difficult to quantify the importance of the eddy field in the large-scale dynamics directly from observations. This quantification is the main goal of the present study.

Here we apply a residual-mean framework to examine whether observations in the BG are consistent with eddies playing a leading order role in the dynamics and transport. The residual-mean circulation is the sum of the mean flow (i.e., the Eulerian-mean circulation) plus transport by eddies (i.e., the bolus transport). This decomposition has proven effective, for example, for understanding Southern Ocean dynamics [Danabasoglu *et al.*, 1996; Marshall and Radko, 2003; Marshall and Speer, 2012]. In the Southern Ocean the wind-driven Deacon Cell is largely balanced by a mesoscale eddy-induced overturning cell, and the residual-mean circulation vanishes. We test the hypothesis that wind driving of the large-scale anticyclonic BG circulation is balanced by eddy fluxes (bolus fluxes). In this balance (shown schematically in Figure 1), the residual-mean circulation is zero; with this starting assumption, a relationship may be derived between lateral eddy diffusivity  $K_D$ , surface-ocean stress, and isopycnal slopes of the large-scale gyre. Observations of the latter two then allow for estimates of  $K_D$ . We go on to compare the spatial patterns and magnitudes of the diffusivities to those computed directly using mixing length theory from timeseries of data from four moorings deployed in the BG.

The paper is set out as follows. In Section 2 we describe BG observations and wind forcing used in the analysis. In Section 3, guided by residual-mean theory, we infer BG halocline eddy diffusivities required to bring the BG residual flow to zero. In Section 4 we show that these estimates are similar to those deduced from mooring data. In Section 5 we conclude with a discussion of the implications of our study.



43 **Figure 1.** Schematic of the hydrography and circulation of the Beaufort Gyre, fresh (blue) at the surface  
 44 and salty (red) below. The grey arrows represent the anticyclonic forcing of the gyre by the prevailing winds.  
 45 The black arrow represents freshwater being gathered towards the center of the gyre by wind-driven Ekman  
 46 transport, the convergence of which pumps down into the center of the gyre. This causes salinity surfaces to  
 47 bow downward into the interior, deep in the center and shallow on the periphery of the gyre. The baroclinic  
 48 instability of the gyre has the tendency to flatten salinity surfaces and results in an eddy bolus flux (black  
 49 arrow) of freshwater directed outward from the center, offsetting the inward flux at the surface.

## 70 2 Observed structure of the Beaufort Gyre and wind forcing

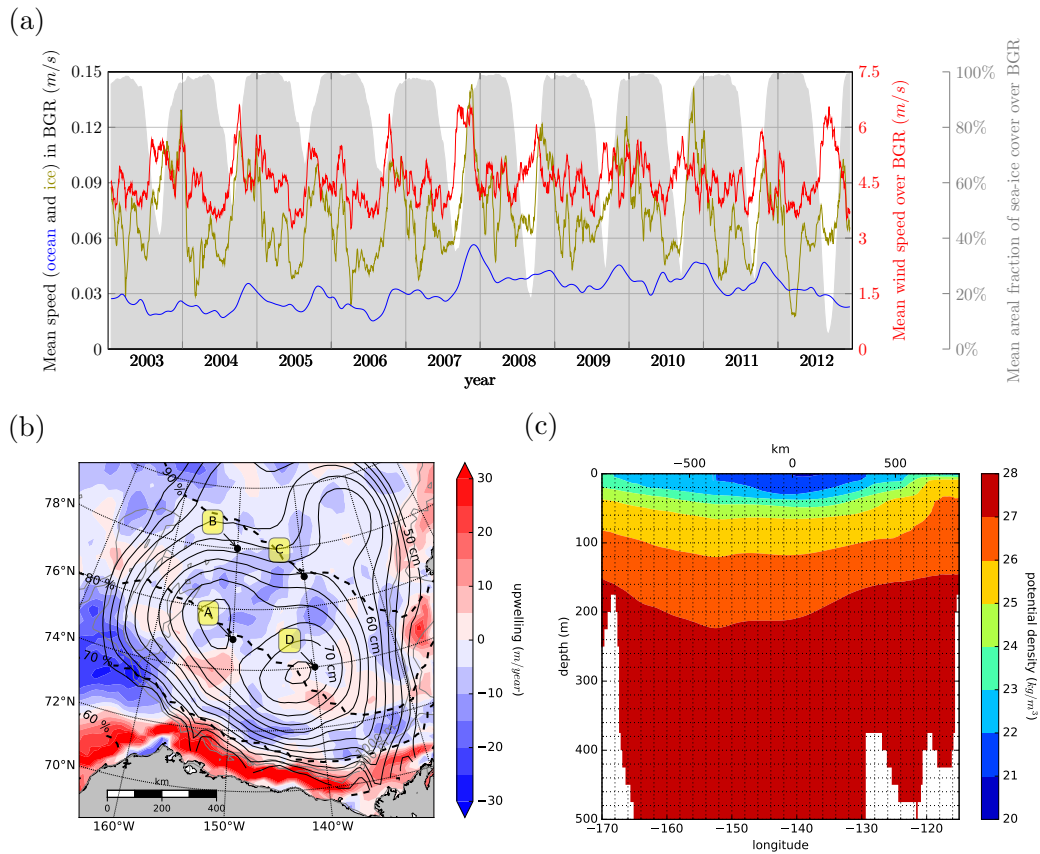
80 Four datasets are combined to estimate the air-ocean and ice-ocean stress  $\boldsymbol{\tau}$  and Ek-  
 81 man pumping  $w_{Ek} = \frac{\nabla \times \boldsymbol{\tau}}{\rho_0 f_0}$ , where  $\rho_0 = 1027.5 \text{ kg m}^{-3}$  is a reference density and  $f_0 =$   
 82  $1.46 \times 10^{-4} \text{ s}^{-1}$  is the Coriolis parameter: (i) sea ice concentration  $\alpha$  from Nimbus-7 SMMR  
 83 and DMSP SSM/I-SSMIS Passive Microwave Data Version 1 [Cavalieri *et al.*, 1996]; (ii)  
 84 sea ice velocity  $\mathbf{u}_{ice}$  from the Polar Pathfinder Daily 20 km EASE-Grid Sea Ice Motion Vec-  
 85 tors, Version 3 [Tschudi *et al.*, 2016]; (iii) surface geostrophic currents  $\mathbf{u}_{geo}$  computed from  
 86 Dynamic Ocean Topography [Armitage *et al.*, 2016, 2017] and (iv) 10 m wind  $\mathbf{u}_{air}$  from  
 87 the NCEP-NCAR Reanalysis 1 [Kalnay *et al.*, 1996]. The 2003-2012 temporal variability of  
 88 these four variables (mean values over the Beaufort Gyre) is summarized in Figure 2a.

89 We follow the approach of Yang [2006, 2009] and compute the mean surface stress  
 90  $\boldsymbol{\tau}$  by averaging daily surface stresses, computed as a combination of ice-ocean and air-ocean  
 91 surface stresses, each estimated using a quadratic drag law with fixed drag coefficients ( $C_{Dice} =$   
 92  $0.0055$ ,  $C_{Dair} = 0.00125$ ), and weighted by the observed local ice concentration  $\alpha$ :

$$93 \boldsymbol{\tau} = \underbrace{\alpha \rho_0 C_{Dice} |\mathbf{u}_{rel}| (\mathbf{u}_{rel})}_{\boldsymbol{\tau}_{ice}} + (1 - \alpha) \underbrace{\rho_{air} C_{Dair} |\mathbf{u}_{air}| (\mathbf{u}_{air})}_{\boldsymbol{\tau}_{air}} \quad (1)$$

94 where the ice-ocean relative velocity  $\mathbf{u}_{rel}$  may be written in terms of the ice velocity  $\mathbf{u}_{ice}$ ,  
 the surface geostrophic velocity  $\mathbf{u}_{geo}$ , and the Ekman velocity  $\mathbf{u}_{Ek}$  as  $\mathbf{u}_{rel} = \mathbf{u}_{ice} - (\mathbf{u}_{geo} + \mathbf{u}_{Ek})$ .

95 Our estimate of the surface ocean current  $\mathbf{u}_{geo} + \mathbf{u}_{Ek}$  differs from Yang [2006, 2009],  
 96 however, in two key ways. First, we use the Ekman velocity at the surface (rotated  $45^\circ$  to  
 97 the right of the surface stress) in place of the mean Ekman transport velocity ( $90^\circ$  from the  
 98 surface stress), thus  $\mathbf{u}_{Ek} = \boldsymbol{\tau} \frac{\sqrt{2} e^{-i\frac{\pi}{4}}}{f_0 \rho_0 D_e}$ , with  $D_e = 20 \text{ m}$  [Yang, 2006]. Second, and more  
 99 importantly, we include the surface geostrophic current  $\mathbf{u}_{geo}$  inferred from dynamic ocean  
 100 topography [McPhee, 2013; Armitage *et al.*, 2016, 2017]. The geostrophic current speed



71 **Figure 2.** (a) Thirty-day running mean of sea-ice speed (green), surface geostrophic current speed (blue)  
 72 and 10 m wind speed (red) over the Beaufort Gyre Region, delimited by 70.5°N-80.5°N and 170°W-130°W  
 73 and including only locations with depths greater than 300 m [Proshutinsky *et al.*, 2009]. The gray shading  
 74 represents mean areal fraction of sea-ice cover. The white annual downward spikes correspond to the sum-  
 75 mertime with progressively less ice cover over time, particularly in 2012. (b) The 2003-2012 climatology  
 76 of Ekman pumping  $w_{Ek}$  (color) and geopotential height  $D$  computed from the 2005-2012 World Ocean At-  
 77 las (WOA) climatology (black contours, see §3); the location of the four Beaufort Gyre Observing System  
 78 moorings (named A, B, C and D) are marked by black dots. (c) hydrographic section of potential density  
 79 (referenced to the surface) at 75°N, computed from the WOA climatology.

101 approximately doubled after 2007 (Figure 2a, blue line), and we find that its inclusion has a  
102 non-negligible influence on Ekman pumping rates.

103 The 2003-2012 average Ekman pumping field inferred from observations (Figure 2b,  
104 color) depends on the prevailing winds and basin geometry, the distribution, drift speed  
105 and concentration of sea ice, and the strength of surface currents. We infer average down-  
106 welling rates of order  $5 \text{ m yr}^{-1}$  within the BG region, but there is considerable spatial struc-  
107 ture. Strong upwelling speeds, in excess of  $30 \text{ m yr}^{-1}$ , can be seen in the coastal areas south  
108 of the 300 m bathymetric contour. Northwards of this downwelling rates reach  $20 \text{ m yr}^{-1}$   
109 corresponding to a mean sea-ice concentration between 65% and 75%. For larger mean ice  
110 concentration, the BG Region is characterized by lower downwelling rates of order  $5 \text{ m yr}^{-1}$ ,  
111 with localized patches of upwelling of maximum  $10 \text{ m yr}^{-1}$  around  $74^\circ\text{N}$ . Note however  
112 that our computations of eddy diffusivity described below depend on integrals over closed  
113 geostrophic contours and so do not depend on many of these details.

114 We remark that, as a consequence of the inclusion of the surface geostrophic current,  
115 our Ekman pumping field differs considerably in both intensity and spatial structure from  
116 previous results, as can be deduced by comparing Figure 2b with the results of *Yang* [2006,  
117 2009] or *McPhee* [2013]. We defer a more detailed discussion of the topic to a subsequent  
118 paper.

119 The hydrographic structure of the BG, based on the quarter-degree resolution 2005-  
120 2012 World Ocean Atlas Climatology [*Locarnini et al.*, 2013; *Zweng et al.*, 2013], is summa-  
121 rized by contours of geopotential height

$$D = \frac{1}{g} \int_0^{p_0} [\rho^{-1}(S, T, p) - \rho^{-1}(35, 0, p)] dp \quad (2)$$

122 where  $\rho^{-1}$  is the specific volume and  $p_0 = 400 \text{ dbar}$  (Figure 2b), and by a section of poten-  
123 tial density across  $75^\circ\text{N}$  (Figure 2c). Potential density increases rapidly from  $1022 \text{ kg m}^{-3}$   
124 to  $1027 \text{ kg m}^{-3}$  over the halocline in the top 300 m to join the very weakly stratified waters  
125 below. As expected from the pattern of Ekman pumping being imposed by the wind from  
126 above, isopycnals are deeper in the middle of the BG, with slopes of the order of 50 m over  
127 500 km or less. This hydrographic structure supports, through thermal wind, the large-scale  
128 anticyclonic circulation of the gyre and is essential to our estimates of the eddy diffusivity  
129 required to balance the effect of the Ekman pumping, as outlined in the next section.

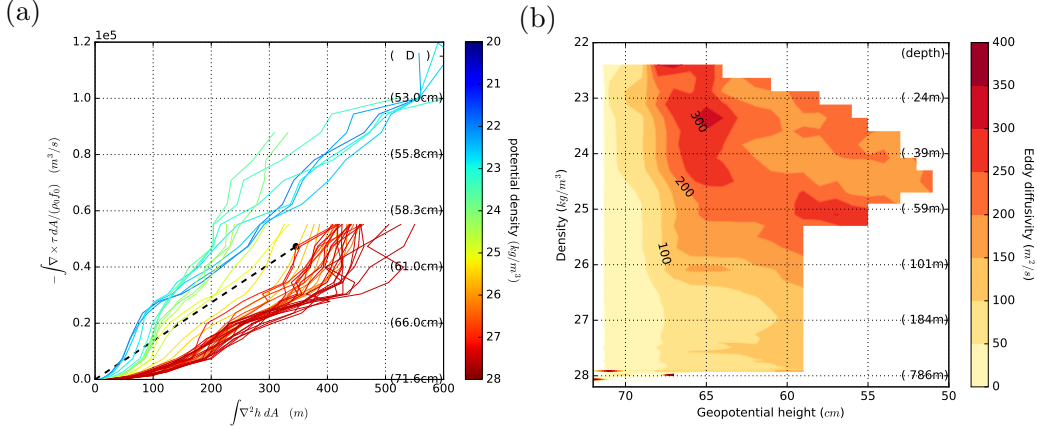
### 130 3 Eddy diffusivities in the limit of vanishing Residual Circulation

131 Adopting a residual mean theory framework [*Andrews and McIntyre*, 1976; *Marshall*  
132 *and Radko*, 2003; *Plumb and Ferrari*, 2005], we now use the observations of Ekman pump-  
133 ing and isopycnal slopes presented in section 2 to infer the magnitude of the eddy diffusiv-  
134 ities required to bring the residual circulation in the halocline of the BG to zero. This is the  
135 limiting case analogous to the ‘vanishing of the Deacon Cell’ in the literature on Southern  
136 Ocean dynamics reviewed by *Marshall and Speer* (2012).

137 We integrate azimuthally along geopotential height contours shown in Figure 2b to rep-  
138 resent the overturning circulation in the  $(r, z)$  plane by a streamfunction:  $(v_r, w) = \left(-\frac{\partial\Psi}{\partial z}, \frac{\partial\Psi}{\partial r}\right)$ ,  
139 where  $r$  is a radial coordinate. In the assumed adiabatic interior of the halocline, we consider  
140 the limit case that the streamfunction describing the residual-mean circulation is vanishingly  
141 small:

$$\Psi_{res} = \bar{\Psi} + \Psi^* = 0, \quad (3)$$

142 where the Eulerian-mean streamfunction is given by the Ekman transport,  $\bar{\Psi} = \bar{\tau}/(\rho_0 f_0)$ ,  
143 and the eddy-induced streamfunction is given by  $\Psi^* = \overline{v'_r b'}/\bar{b}_z$ , where  $\overline{v'_r b'}$  is the radial  
144 eddy buoyancy flux and  $\bar{b}_z$  is the vertical stratification. Overbars denote time and along-  
145 geopotential-height-contour averages. We are computing, then, the limit case in which bolus



161 **Figure 3.** (a) Integrated Ekman pumping (in  $\text{m}^3 \text{s}^{-1}$ ) plotted against the integrated  $\nabla^2 h$  (in m) at different  
 162 density levels as indicated by color. The resulting eddy diffusivity  $K_D$  can be readily obtained as the ratio of  
 163 the two values, equivalent to the slope of the dotted line (in  $\text{m}^2 \text{s}^{-1}$ ). (b) Eddy diffusivity  $K_D$  as a function of  
 164 density and geopotential height contour; the depth in parenthesis is the mean depth of the isopycnal.

146 transport by eddies are sufficiently strong to exactly balance the Eulerian-mean flow set up by  
 147 the wind.

148 As is conventional (see Gent and McWilliams, 1991) we characterise the efficiency of  
 149 eddy transport by an eddy diffusivity and write,  $v'_r b' = -K_D \bar{b}_r$ , and so  $\Psi^* = -K_D \bar{b}_r / \bar{b}_z$ .  
 150 Adopting this closure as our definition of diffusivity, Eq.(3) provides a relationship between  
 151 the wind stress  $\bar{\tau}$ , the mean buoyancy variations  $\bar{b}_r$  and  $\bar{b}_z$ , and the eddy diffusivity  $K_D$

$$K_D = \frac{1}{\rho_0 f_0} \frac{\bar{\tau}}{\bar{s}} \quad \text{where} \quad \bar{s} = -\frac{\bar{b}_r}{\bar{b}_z} = \frac{\partial \bar{h}}{\partial r}. \quad (4)$$

152 Here  $h$  is the depth of the isopycnal,  $r$  is the radial coordinate and  $\bar{s}$  the slope of the isopycnal  
 153 of the time and azimuthally averaged density field. For computational convenience, rather  
 154 than integrating along geopotential height contours, we use the divergence and Stokes theo-  
 155 rems to rewrite (4) as

$$K_D = \frac{1}{\rho_0 f_0} \frac{\int \nabla \times \tau dA}{\int \nabla^2 h dA}, \quad (5)$$

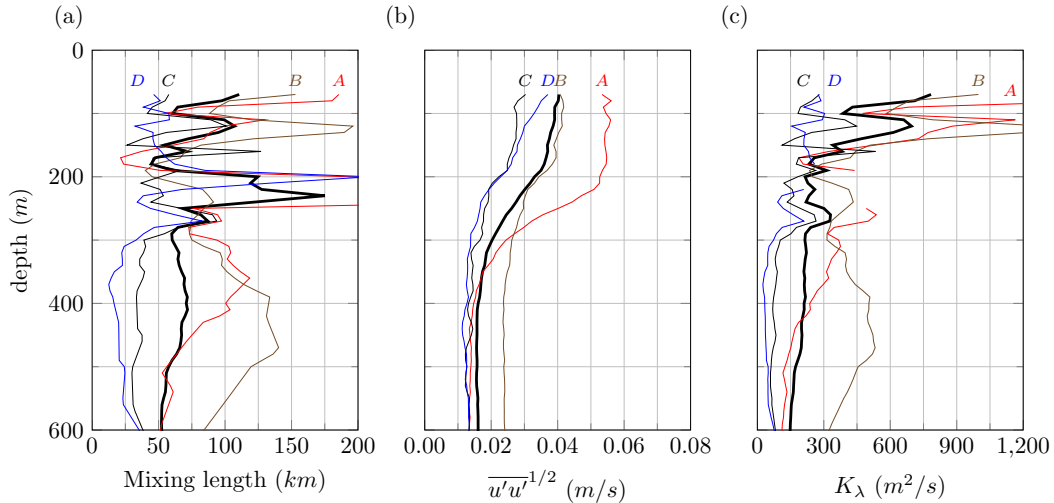
156 where the integrals are performed over the area circumscribed by a geopotential height con-  
 157 tour, and  $\tau$  and  $h$  are averaged only in time. The integrated Ekman pumping (in  $\text{m}^3 \text{s}^{-1}$ ) and  
 158 thickness flux (m), i.e. the numerator and denominator of (5) respectively, are plotted in Fig-  
 159 ure 3a for different density levels. The slope of the dotted line plotted in Figure 3a yields the  
 160 diffusivity for the point marked with a dot, as given by (4).

165 The estimated eddy diffusivity, ranging from  $50 \text{ m}^2 \text{ s}^{-1}$  to  $400 \text{ m}^2 \text{ s}^{-1}$ , is plotted as a  
 166 function of geopotential height and density in Figure 3b. We observe a strong dependence on  
 167 the density level and on the geopotential height contour: higher values of eddy diffusivity are  
 168 concentrated in the top 100 m from the surface (lighter than  $26 \text{ kg m}^{-3}$ , see also Figure 2c)  
 169 and close to the 65 cm geopotential height contour, and decay by a factor of four at greater  
 170 depth and towards the center of the gyre. White areas in Figure 3b correspond to outcrop-  
 171 ping isopycnals above  $25 \text{ kg m}^{-3}$  and/or to the presence of land in at least one point along the  
 172 dynamic height contour below that.

173 We remark that uncertainty in the evaluation of the numerator and denominator of (4)  
 174 is large. There are errors in our estimates of stress due to uncertainties in Ekman layer thick-  
 175 ness  $D_e$ , the drag coefficients  $C_{Dice}$  and  $C_{Dair}$  as well as in the accuracy of the estimated  
 176 ice, wind and ocean surface velocities. As an example, decreasing (increasing) the Ekman  
 177 layer thickness from 20 m [Yang, 2006] to 10 m (40 m) [Cole *et al.*, 2017] results in a de-  
 178 crease (increase) of the estimated eddy diffusivity by approximately 20%. Similarly, there  
 179 are uncertainties in the ice-ocean drag coefficient, which can vary between 0.001 and 0.01  
 180 depending on ice roughness, concentration and many other factors [Lu *et al.*, 2011; Cole  
 181 *et al.*, 2017]. A possibly even larger source of uncertainty is associated with the wind, ice  
 182 and ocean velocities used in (1). Before we go on we should note that if the mean Ekman  
 183 pumping over the region were  $10 \text{ m yr}^{-1}$  instead of  $5 \text{ m yr}^{-1}$ , the eddy diffusivity required to  
 184 bring the residual flow to zero would be doubled.

185 The values of  $K_D$  shown in Figure 3 are those required to exactly balance Ekman pro-  
 186 cesses. So, how large might we expect lateral eddy diffusivities to be? To explore we now  
 187 estimate lateral diffusivity using an entirely different method making use of hydrographic  
 188 and current meter data.

#### 189 4 Estimates of eddy diffusivities from mooring data



190 **Figure 4.** Profiles of a) mixing length, b) magnitude of velocity fluctuations, and c) along-isopycnal eddy  
 191 diffusivity  $K_\lambda$  at the four BGOS moorings. The black thick line denotes the mean among the four moorings.  
 192 Extraneous mixing lengths at moorings A and D (red and blue) over 200-250 m depth are excluded from the  
 193 diffusivity calculation (see text).

194 Horizontal eddy diffusivity is estimated from temperature, salinity and velocity pro-  
 195 files obtained from four Beaufort Gyre Observing System (BGOS) moorings, whose position  
 196 are shown in Figure 2b. A mixing length framework is employed as described by Cole *et al.*  
 197 [2015]. Each mooring provides a pair of profiles spanning  $\approx 50 \text{ m}$  to  $2000 \text{ m}$  depth every 54  
 198 hours. Each pair of profiles is separated by 6 hours in time so that averaging minimizes the  
 199 influence of near-inertial motions that have an approximately 12 hour period. Processed data  
 200 have a 2 m vertical resolution. Data are utilized over August 2003 to August 2012, with each  
 201 mooring having some years in which data were not returned (e.g., mooring A: July 2006  
 202 – Aug 2007 and July 2008 – September 2009). The record at mooring C ended in August  
 203 2007. Monthly mapped temperature and salinity fields from the MIMOC climatology are

204 also utilized, which are estimated directly on density surfaces at 0.5° resolution [*Schmidtko*  
205 *et al.*, 2013].

206 The mixing length,  $\lambda$ , and horizontal diffusivity,  $K_\lambda$ , are estimated as:

$$\lambda = \frac{\overline{\theta'_{iso} \theta'_{iso}}^{1/2}}{|\nabla \overline{\theta_{iso}}|} \quad (6)$$

$$K_\lambda = c_0 \lambda \overline{u'u'}^{1/2} \quad (7)$$

207 where  $\theta_{iso}$  is the temperature along a density surface,  $u$  the horizontal velocity vector, and  
208  $c_0$  a mixing efficiency [*Tennekes*, 1972; *Armi and Stommel*, 1983; *Naveira Garabato et al.*,  
209 2011; *Abernathy and Cessi*, 2014]. The mixing efficiency is taken to be  $c_0 = 0.16$  [*Wunsch*,  
210 1999; *Klocker and Abernathy*, 2014]. Primed quantities denote a fluctuation from the mean;  
211 temperature and velocity were first averaged with a 30-day timescale, and then all variability  
212 at timescales larger than one year was removed. The timescales are chosen to exclude higher  
213 frequency variability primarily in the velocity observations, and to represent the mesoscale  
214 dynamics of the system. Overbar denotes a temporal average over all years. The spatial gra-  
215 dient of the mean temperature field,  $\nabla \overline{\theta_{iso}}$ , is estimated along density surfaces from MIMOC  
216 [*Schmidtko et al.*, 2013] at a 100 km scale. The calculation is performed independently on  
217 each density surface and for each mooring. Only the upper 600 m are presented here.

218 The mixing length framework assumes that temperature and salinity anomalies along a  
219 density surface are determined by horizontal processes, and that vertical processes are neg-  
220 ligible. Two of the moorings, *A* and *D*, fail this criteria in the 200-250 m depth range where  
221 horizontal gradients are very small; these regions lead to an elevated mixing length (Fig-  
222 ure 4a), and are excluded from the horizontal diffusivity estimate (Figure 4c).

223 A range of mixing lengths, velocity fluctuations, and diffusivities were found at the  
224 four moorings (Figure 4). Mixing length values ranged from less than 50 to near 200 km.  
225 Velocity fluctuations decayed by more than a factor of two between 70 m and 300 m depth,  
226 and then remained constant at approximately  $0.02 \text{ m s}^{-1}$ . Both mixing length and velocity  
227 fluctuations are small in comparison to other regions [*Cole et al.*, 2015]. Eddy diffusivities  
228 ranged from 100 to more than  $600 \text{ m}^2 \text{ s}^{-1}$ , with a factor of two decay with depth from 70 to  
229 300 m arising from that of the velocity fluctuations. There was significant variability in all  
230 quantities between the moorings, with mooring B having elevated mixing lengths, velocity  
231 fluctuations, and diffusivity at all depths due to its proximity to the basin boundary and the  
232 Chukchi Plateau, a source of eddies that transit past mooring B [*Carpenter and Timmermans*,  
233 2012].

234 There are considerable uncertainties in our evaluation of  $K_\lambda$ . The mixing length is not  
235 always well conditioned, as seen for example for moorings A and D. Eddy kinetic energy  
236 depends on the period over which the cutoff is applied; here we have chosen 30 days, but  
237 higher EKE is obtained for higher frequency cutoffs. As an example, a 7 days cutoff results  
238 in an approximately 30% larger EKE and eddy diffusivity. The value of  $c_0$ , here set to 0.16,  
239 depends on the decorrelation timescale of the eddies which could very well be different in  
240 the Arctic from elsewhere. Nevertheless, despite the uncertainties our estimates of  $K_\lambda$  and  
241  $K_D$ , they are broadly similar to one-another, both in magnitude and in space.

## 242 5 Discussion and implications

243 Guided by residual mean theory and the observed structure of the halocline in the BG,  
244 we have mapped out the magnitude and spatial pattern of eddy diffusivity required to ex-  
245 actly balance the Eulerian-mean flow set up by winds (Ekman processes mediated by ice)  
246 blowing over the surface. We find eddy diffusivities  $K_D$  that vary from order  $400 \text{ m}^2 \text{ s}^{-1}$  at  
247 the surface decaying rapidly over the halocline to order  $50 \text{ m}^2 \text{ s}^{-1}$  at a depth of 300 m or so,



and close to the center of the gyre. We remark that both the eddy diffusivity value and its spatial structure are in agreement with results from eddy resolving numerical simulation by *Manucharyan et al.* [2016] (see Figure 3 of that paper), having comparable surface stresses of order  $0.01 \text{ N m}^{-2}$ .

Estimates of eddy diffusivity  $K_\lambda$ , employing mixing length theory based on BG mooring measurements, are at least as large as  $K_D$ , with broadly the same vertical structure. Despite significant uncertainties in both estimates of  $K_\lambda$  and  $K_D$ , our results indicate that the eddy-induced transport in the BG is of the same order of magnitude as that required to balance the accumulation of freshwater by Ekman pumping, estimated using surface stress climatology.

This has the following implications:

1. freshwater, heat and tracer transport in the BG, which is achieved by the residual flow, is likely very different from that based on the Eulerian mean circulation, the quantity conventionally mapped from observations.
2. if the residual overturning circulation is indeed small in the halocline, then its depth  $H$  will scale as (from Eq.4)  $H \simeq \frac{R\tau}{\rho_0 f_0 K_D}$ , where  $R$  is the radius of the gyre. This is the scaling for the depth of the thermocline in the ACC postulated by *Marshall and Radko* [2003] and the depth of the halocline found by *Manucharyan et al.* [2016] and *Manucharyan and Spall* [2016] in their idealized models of the BG.
3. models of the Arctic require a mesoscale parameterization with diffusivities around  $500 \text{ m}^2 \text{ s}^{-1}$  decaying over the depth of the halocline to small values in the abyss.
4. how models respond to a change in the wind may be dependent on how they parameterize mesoscale eddies, since eddies play a zero-order role in mediating the freshwater budget of the gyre.

Future work should attempt to constrain more precisely the estimates presented here. Perhaps the most direct approach would be to carry out a tracer release in the halocline of the BG following the example of the DIMES experiment [*Gille et al.*, 2012] in the Southern Ocean. The rates of lateral and vertical dispersion can then yield direct information about mesoscale eddy stirring rates and diapycnal mixing rates.

## Acknowledgments

We thank Jean-Michel Campin, Edward Dorridge, Andrey Proshutinsky and Miles McPhee for their help and insights. The experiments described here were made possible by support from the NSF program in Arctic Research, Award Number 1603557. STC was supported through NSF award numbers 1355668 and 1602926.

NCEP Reanalysis data provided by the NOAA/OAR/ESRL PSD, Boulder, Colorado, USA, from their Web site at <http://www.esrl.noaa.gov/psd/> [*Kalnay et al.*, 1996]

Arctic dynamic topography data were provided by the Centre for Polar Observation and Modelling, University College London [www.cpom.ucl.ac.uk/dynamic\\_topography](http://www.cpom.ucl.ac.uk/dynamic_topography) [*Armitage et al.*, 2016]

BG mooring data were collected and made available by the Beaufort Gyre Exploration Program based at the Woods Hole Oceanographic Institution (<http://www.whoi.edu/beaufortgyre>) in collaboration with researchers from Fisheries and Oceans Canada at the Institute of Ocean Sciences. Data are online at: <http://www.whoi.edu/website/beaufortgyre/data>.

## References

- 291  
292 Abernathey, R., and P. Cessi (2014), Topographic Enhancement of Eddy Efficiency in  
293 Baroclinic Equilibration, *Journal of Physical Oceanography*, *44*(8), 2107–2126, doi:  
294 10.1175/JPO-D-14-0014.1.
- 295 Andrews, D. G., and M. E. McIntyre (1976), Planetary Waves in Horizontal and Ver-  
296 tical Shear: The Generalized Eliassen-Palm Relation and the Mean Zonal Accel-  
297 eration, *Journal of the Atmospheric Sciences*, *33*, 2031–2048, doi:10.1175/1520-  
298 0469(1976)033<2031:PWIHAV>2.0.CO;2.
- 299 Armi, L., and H. Stommel (1983), Four Views of a Portion of the North Atlantic Sub-  
300 tropical Gyre, *Journal of Physical Oceanography*, *13*(5), 828–857, doi:10.1175/1520-  
301 0485(1983)013<0828:FVOAPO>2.0.CO;2.
- 302 Armitage, T. W. K., S. Bacon, A. L. Ridout, S. F. Thomas, Y. Aksenov, and D. J. Wingham  
303 (2016), Arctic sea surface height variability and change from satellite radar altimetry and  
304 GRACE, 2003–2014, *Journal of Geophysical Research: Oceans*, *121*(6), 4303–4322, doi:  
305 10.1002/2015JC011579.
- 306 Armitage, T. W. K., S. Bacon, A. L. Ridout, A. A. Petty, S. Wolbach, and M. Tsamados  
307 (2017), Arctic Ocean geostrophic circulation 2003–2014, *The Cryosphere Discussions*,  
308 *2017*, 1–32, doi:10.5194/tc-2017-22.
- 309 Carpenter, J. R., and M.-L. Timmermans (2012), Deep mesoscale eddies in the  
310 Canada Basin, Arctic Ocean, *Geophysical Research Letters*, *39*(20), 1–6, doi:  
311 10.1029/2012GL053025.
- 312 Cavaleri, D. J., C. L. Parkinson, P. Gloersen, and H. J. Zwally (1996), Sea Ice Concentra-  
313 tions from Nimbus-7 SMMR and DMSP SSM/I-SSMIS Passive Microwave Data, Version  
314 1, doi:10.5067/8GQ8LZQVL0VL.
- 315 Cole, S. T., C. Wortham, E. Kunze, and W. B. Owens (2015), Eddy stirring and horizontal  
316 diffusivity from Argo float observations: Geographic and depth variability, *Geophysical*  
317 *Research Letters*, *42*(10), 3989–3997, doi:10.1002/2015GL063827.
- 318 Cole, S. T., J. M. Toole, R. Lele, M. L. Timmermans, S. G. Gallaher, T. P. Stanton, W. J.  
319 Shaw, B. Hwang, T. Maksym, J. P. Wilkinson, M. Ortiz, H. Graber, L. Rainville, A. A.  
320 Petty, S. L. Farrel, J. A. Richter-Menge, and C. Haas (2017), Ice and ocean velocity in the  
321 Arctic marginal ice zone: Ice roughness and momentum transfer, *Elementa: Science of the*  
322 *Anthropocene*, *in press*.
- 323 Danabasoglu, G., J. C. McWilliams, and W. G. Large (1996), Approach to equilibrium in ac-  
324 celerated global oceanic models, *Journal of Climate*, *9*(5), 1092–1110, doi:10.1175/1520-  
325 0442(1996)009<1092:ATEIAG>2.0.CO;2.
- 326 Gille, S., J. R. Ledwell, A. C. Naveira Garabato, K. Speer, D. Balwada, A. Brearley, J. B.  
327 Girton, A. Griesel, R. Ferrari, A. Klocker, J. H. LaCasce, P. Lazarevich, N. Mackay, M. P.  
328 Meredith, M.-J. Messias, B. Owens, J.-B. Sallée, K. Sheen, E. Shuckburgh, D. A. Smeed,  
329 L. C. St-Laurent, J. M. Toole, A. J. Watson, N. Wienders, and U. Zajaczkovski (2012), The  
330 Diapycnal and Isopycnal Mixing Experiment: A First Assessment, *J. Phys. Oceanogr.*,  
331 *17*(58), 2009–2011, doi:10.1029/2009JC005821.CLIVAR.
- 332 Kalnay, E., M. Kanamitsu, R. Kistler, W. Collins, D. Deaven, L. Gandin, M. Iredell, S. Saha,  
333 G. White, J. Woollen, Y. Zhu, M. Chelliah, W. Ebisuzaki, W. Higgins, J. Janowiak, K. C.  
334 Mo, C. Ropelewski, J. Wang, A. Leetmaa, R. Reynolds, R. Jenne, and D. Joseph (1996),  
335 The NCEP/NCAR 40-year reanalysis project, *Bulletin of the American Meteorological*  
336 *Society*, *77*(3), 437–471, doi:10.1175/1520-0477(1996)077<0437:TNYRP>2.0.CO;2.
- 337 Klocker, A., and R. Abernathey (2014), Global Patterns of Mesoscale Eddy Properties and  
338 Diffusivities, *Journal of Physical Oceanography*, *44*(3), 1030–1046, doi:10.1175/JPO-D-  
339 13-0159.1.
- 340 Locarnini, R. A., A. V. Mishonov, J. I. Antonov, T. P. Boyer, H. E. Garcia, O. K. Bara-  
341 nova, M. M. Zweng, C. R. Paver, J. R. Reagan, D. R. Johnson, M. Hamilton, and D. Sei-  
342 dov (2013), World Ocean Atlas 2013. Vol. 1: Temperature., *Tech. Rep. September*, doi:  
343 10.1182/blood-2011-06-357442.

- 344 Lu, P., Z. Li, B. Cheng, and M. Leppäranta (2011), A parameterization of the ice-  
 345 ocean drag coefficient, *Journal of Geophysical Research*, *116*(C7), C07,019, doi:  
 346 10.1029/2010JC006878.
- 347 Manley, T. O., and K. Hunkins (1985), Mesoscale Eddies of the Arctic Ocean, *Journal of*  
 348 *Geophysical Research C Oceans*, *90*(C3), 19, doi:10.1029/JC090iC03p04911.
- 349 Manucharyan, G. E., and M. A. Spall (2016), Wind-driven freshwater buildup and release  
 350 in the Beaufort Gyre constrained by mesoscale eddies, *Geophysical Research Letters*, doi:  
 351 10.1002/2015GL065957.
- 352 Manucharyan, G. E., M. A. Spall, and A. F. Thompson (2016), A Theory of the Wind-Driven  
 353 Beaufort Gyre Variability, *Journal of Physical Oceanography*, (2013), 3263–3278, doi:  
 354 10.1175/JPO-D-16-0091.1.
- 355 Marshall, J., and T. Radko (2003), Residual-Mean Solutions for the Antarctic Circumpolar  
 356 Current and Its Associated Overturning Circulation, *Journal of Physical Oceanography*,  
 357 *33*(11), 2341–2354, doi:10.1175/1520-0485(2003)033<2341:RSFTAC>2.0.CO;2.
- 358 Marshall, J., and K. Speer (2012), Closure of the meridional overturning circulation through  
 359 Southern Ocean upwelling, *Nature Geoscience*, *5*(3), 171–180, doi:10.1038/ngeo1391.
- 360 McPhee, M. G. (2013), Intensification of geostrophic currents in the Canada Basin, Arctic  
 361 Ocean, *Journal of Climate*, *26*(10), 3130–3138, doi:10.1175/JCLI-D-12-00289.1.
- 362 Naveira Garabato, A. C., R. Ferrari, and K. L. Polzin (2011), Eddy stirring in the Southern  
 363 Ocean, *Journal of Geophysical Research: Oceans*, *116*(9), doi:10.1029/2010JC006818.
- 364 Plumb, R. A., and R. Ferrari (2005), Transformed Eulerian-Mean Theory. Part I: Nonquasi-  
 365 geostrophic Theory for Eddies on a Zonal-Mean Flow, *Journal of Physical Oceanography*,  
 366 *35*(2), 165–174, doi:10.1175/JPO-2669.1.
- 367 Proshutinsky, A., R. Krishfield, M.-I. Timmermans, J. Toole, E. Carmack, F. Mclaughlin,  
 368 W. J. Williams, S. Zimmermann, M. Itoh, and K. Shimada (2009), Beaufort Gyre freshwa-  
 369 ter reservoir : State and variability from observations, *Journal of Geophysical Research*,  
 370 *114*, 1–25, doi:10.1029/2008JC005104.
- 371 Proshutinsky, A., D. Dukhovskoy, M.-I. Timmermans, R. Krishfield, and J. L. Bamber  
 372 (2015), Arctic circulation regimes, *Philosophical transactions. Series A, Mathematical,*  
 373 *physical, and engineering sciences*, *373*(2052), 20140,160, doi:10.1098/rsta.2014.0160.
- 374 Proshutinsky, A. Y., and M. A. Johnson (1997), Two circulation regimes of the wind-driven  
 375 Arctic Ocean, *Journal of Geophysical Research: Oceans*, *102*(C6), 12,493–12,514, doi:  
 376 10.1029/97JC00738.
- 377 Schmidtko, S., G. C. Johnson, and J. M. Lyman (2013), MIMOC: A global monthly isopy-  
 378 cnal upper-ocean climatology with mixed layers, *Journal of Geophysical Research:*  
 379 *Oceans*, *118*(4), 1658–1672, doi:10.1002/jgrc.20122.
- 380 Tennekes, H. (1972), *A First Course in Turbulence*, 300 pp., doi:  
 381 10.1017/S002211207321251X.
- 382 Timmermans, M.-L., J. Toole, A. Proshutinsky, R. Krishfield, and A. Plueddemann (2008),  
 383 Eddies in the Canada Basin, Arctic Ocean, Observed from Ice-Tethered Profilers, *Journal*  
 384 *of Physical Oceanography*, *38*(1), 133–145, doi:10.1175/2007JPO3782.1.
- 385 Tschudi, M., C. Fowler, J. S. Maslanik, and W. Meier (2016), Polar Pathfinder Daily 25 km  
 386 EASE-Grid Sea Ice Motion Vectors, Version 3., doi:10.5067/O57VAIT2AYYY.
- 387 Wunsch, C. (1999), Where do ocean eddy heat fluxes matter?, *Journal of Geophysical Re-*  
 388 *search: Oceans*, *104*(C6), 13,235–13,249, doi:10.1029/1999JC900062.
- 389 Yang, J. (2006), The seasonal variability of the Arctic Ocean Ekman transport and its role  
 390 in the mixed layer heat and salt fluxes, *Journal of Climate*, *19*(20), 5366–5387, doi:  
 391 10.1175/JCLI3892.1.
- 392 Yang, J. (2009), Seasonal and interannual variability of downwelling in the Beaufort Sea, *J*  
 393 *Geophys Res*, *114*, C00A14, doi:10.1029/2008JC005084.
- 394 Zhao, M., M. L. Timmermans, S. Cole, R. Krishfield, A. Proshutinsky, and J. Toole (2014),  
 395 Characterizing the eddy field in the Arctic Ocean halocline, *Journal of Geophysical Re-*  
 396 *search C: Oceans*, *119*(12), 8800–8817, doi:10.1002/2014JC010488.

- 397 Zhao, M., M. L. Timmermans, S. Cole, R. Krishfield, and J. Toole (2016), Evolution of the  
398 eddy field in the Arctic Ocean's Canada Basin, 2005–2015, *Geophysical Research Let-*  
399 *ters*, 43(15), 8106–8114, doi:10.1002/2016GL069671.
- 400 Zweng, M. M., J. Reagan, J. Antonov, A. Mishonov, T. Boyer, H. Garcia, O. Baranova,  
401 D. Johnson, D. Seidov, and M. Bidlle (2013), World Ocean Atlas 2013, Volume 2: Salin-  
402 ity, *Tech. Rep. 1*, doi:10.1182/blood-2011-06-357442.